The Terahertz Atmosphere

Scott Paine, Raymond Blundell
Smithsonian Astrophysical Observatory
Harvard-Smithsonian Center for Astrophysics
60 Garden Street, Cambridge, MA 02138 USA

Abstract

The recent development of sites in unusually high and dry locations, notably the Atacama desert of northern Chile and the South Pole, has extended the range of ground-based radio astronomy to frequencies beyond 1 THz. Instruments for observations at these frequencies are being planned, or are under development, for several telescopes. One experimental telescope, the SAO Submillimeter Receiver Laboratory's RLT, has operated routinely above 1 THz since late 2002.

Observations at these frequencies, where atmospheric attenuation is always high, require a good understanding of the propagation path to be successful. We have spent several years investigating terahertz atmospheric propagation from two sites in northern Chile—the Atacama Large Millimeter Array (ALMA) site near Cerro Chajnantor, and the site of the RLT on Cerro Sairecabur. Using an automated Fourier transform spectrometer (FTS), a large volume of atmospheric emission spectra, covering 300 GHz – 3.5 THz, has been obtained from these sites under a full range of meteorological conditions. As part of this effort, we have developed a general-purpose atmospheric model for terahertz frequencies which is well-validated by these data. We continue to operate the FTS in conjunction with the RLT, and have found that the combined measurement and modeling capability is invaluable for calibrating the astronomical observations.

In this paper, we discuss the observed characteristics of these sites, modeling methods and results, and the use of the FTS as a calibration tool for radio astronomy.

1. Introduction

Ground-based radio astronomy at terahertz frequencies is developing rapidly. Instruments already in operation include the RLT (Blundell et al. 2003), a 0.8 metre terahertz telescope operating on Cerro Sairecabur in northern Chile since 2002, and the TREND receiver (Yngvesson et al. 2004) recently tested on the 1.7 metre AST/RO telescope (Stark, et al. 2001) at the South Pole. THz receivers are planned for the 12 metre APEX telescope near the Atacama Large Millimeter Array (ALMA) site near Cerro Chajnantor in Chile. Meanwhile, Submillimeter interferometry has been extended to 690 GHz by the Submillimeter Array (SMA) on Mauna Kea, Hawaii.

At these frequencies, the observer has to contend with significant atmospheric attenuation. For example, the RLT typically observes in the 1030 GHz atmospheric window with a zenith atmospheric transmittance of 20%, and a system temperature of order 20,000 K. Under these conditions, calibration of the atmospheric attenuation by the usual sky dip method is not feasible, both because of the poor signal to noise ratio (Marrone 2004), and because the approximation of the atmosphere as a single isothermal, isobaric slab may not be valid.

At the RLT, the solution to these difficulties has been to operate a zenith-looking Fourier transform spectrometer (FTS) in conjunction with the astronomical observations. This instrument was originally developed for the SAO Submillimeter Receiver Lab's terahertz site testing program (Paine et al. 2000). The broadband (300 GHz – 3.5 THz) emission spectra produced by the FTS enable accurate calibration of the atmospheric transmission. This capability is enhanced by fitting the emission spectrum using an atmospheric model, which can in turn be used to calculate the atmospheric transmission at full resolution.

This paper presents an overview of the characteristics of the atmosphere over terahertz observatory sites. Examples are presented of emission spectra and model fits for two sites: Sairecabur and Chajnantor. Finally, the use of FTS spectra in conjunction with model fits for calibration of the atmosphere is discussed.

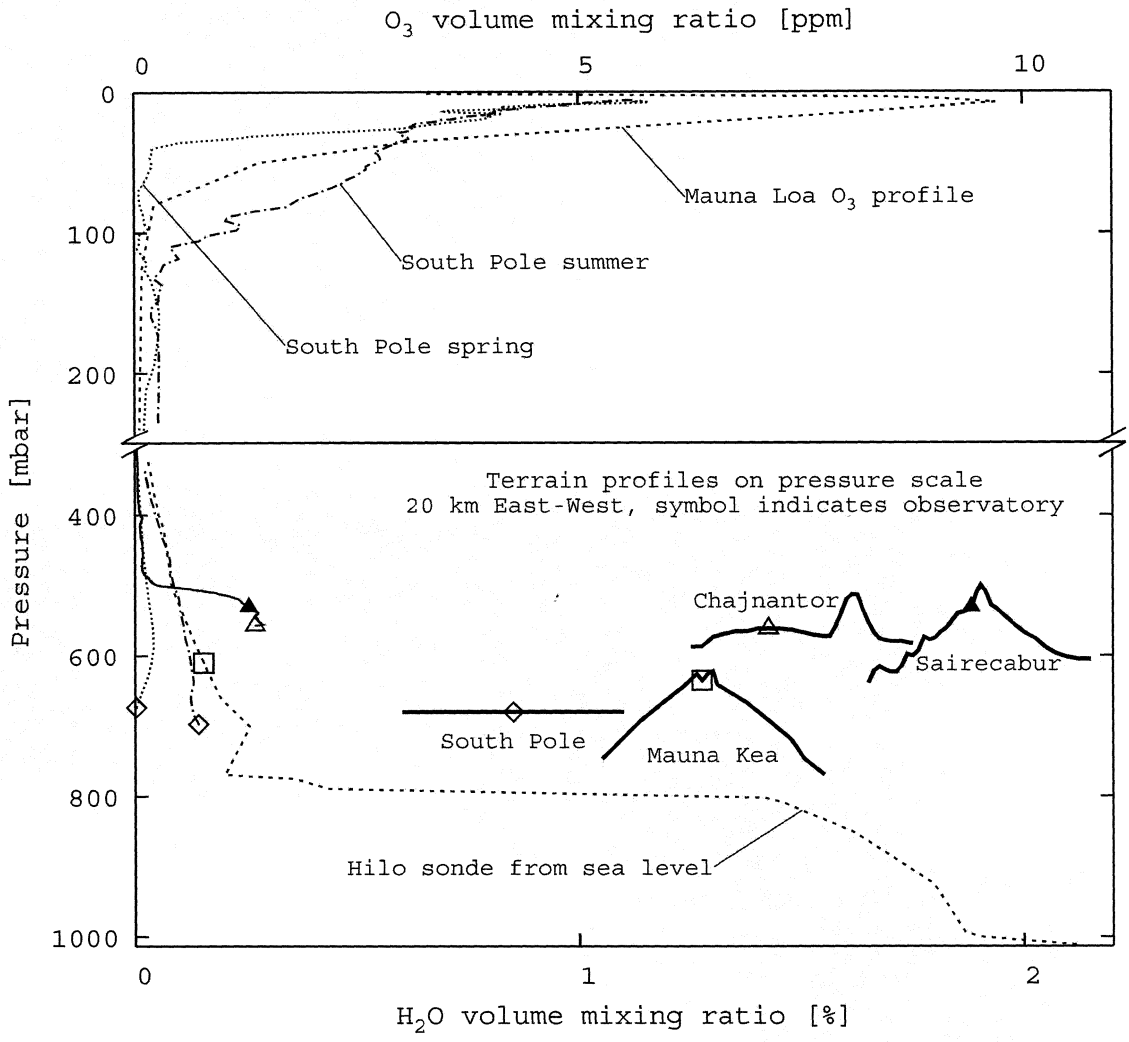

Fig. 2.1 – Vertical profiles of water vapor and ozone above terahertz observatory sites. Symbols indicate the observatory pressure altitudes on the terrain profiles and on the H_2O mixing ratio profiles. Mixing ratio data are from particular soundings which are representative of typical conditions. South Pole data are courtesy of the National Oceanic and Atmospheric Administration (NOAA) Climate Monitoring and Diagnostics Laboratory, Boulder, Colorado, and are from launches on 7 Oct 2003, just before the spring equinox, and in the summer on 29 Dec 2003. The Mauna Loa ozone profile is derived from data in MacDermid (1999). Hilo sonde data are courtesy of the Department of Atmospheric Science, University of Wyoming, for a sonde launched 15 Jan 2003. Chajnantor sonde data here and in Fig. 3.3 are from a series of launches on 10 Nov 1999 as part of collaboration between Cornell University, the European Southern Observatory (ESO), the National Radio Astronomy Observatory (NRAO), and SAO.

2. Characteristics of Observing Sites

The greatest contribution to the atmospheric opacity at terahertz frequencies is from rotation lines of water vapor. These are pressure broadened in the lower troposphere to linewidths of order 3 GHz, and, even at the low column densities encountered above a good terahertz site (0.2 mm – 1 mm precipitable water vapor, or pwv), the strongest

lines are further saturation broadened to many tens of GHz. The weak spin-rotation lines of O_2 contribute significant opacity within a few GHz of these lines. Rotation lines of stratospheric ozone, which have much narrower pressure-broadened linewidths of order 10 MHz, can be a significant factor when these fall close to the observing frequency, or its image in a DSB receiver. In addition to line absorption, short-range collisions among N_2, O_2, and H_2O, produce broad, unresolved continua peaking near 3 THz. A thorough discussion of the roles of these and other atmospheric constituents may be found in Goody & Yung (1989), and references therein.

2.1 Vertical profiles of water vapor and ozone

Fig. 2.1 illustrates typical vertical profiles of water vapor and ozone above four principal sites for terahertz astronomy. The profiles shown are from particular radiosonde flights, but represent typical conditions at each of these sites. By plotting mixing ratio against pressure, the area to the left of each profile is directly proportional to the column density of the plotted species. For comparison, the geographic relief of the sites is plotted on the same vertical pressure scale.

Besides being at high altitude, each of these sites achieves typically low precipitable water vapor (pwv) by different means. At the South Pole, despite the fact that humidity is close to saturation in the lower atmosphere, the water vapor mixing ratio is nevertheless very low by virtue of the extreme cold (Chamberlin 2001). The water vapor profiles presented Fig. 2.1 for the South Pole are the saturated H_2O mixing profiles based on temperature data. Mauna Kea, on the island of Hawaii, presents an entirely different scenario. During good observing weather, humid air at lower levels is trapped under an inversion below summit level. Above the inversion, the air is dry, and the water vapor density typically falls off gradually with altitude. Chajnantor and Sairecabur are located in the dry Atacama climate of northern Chile. During good conditions at Chajnantor, a typical situation is for moderately low humidity at ground level to persist up to an inversion 0.5 – 2 km above ground level, above which the relative humidity level drops to extremely dry levels of a few percent or less. This characteristic was the basis for locating the RLT on Sairecabur, 0.5 km above the ALMA site at Chajnantor.

Representative ozone profiles for the South Pole and Hawaii are shown in the upper part of Fig. 2.1. For northern Chile, local ozone profile measurements have not been made, but the profile is expected to be similar to Hawaii (Andrews 2000). The difference between the spring and summer South Pole ozone profiles is the Antarctic spring ozone hole phenomenon.

As Fig. 2.1 illustrates, these two variable atmospheric constituents, water vapor and ozone, are well-separated vertically. Moreover, while the water vapor distribution varies rapidly on the length and time scales associated with turbulent air movement in the troposphere, ozone varies more slowly over the synoptic length scales associated with the stratosphere. These observations have motivated a recent proposal to use stratospheric ozone line emission as a calibration source to correct for tropospheric phase fluctuations, associated with water vapor, over radio interferometers (Paine 2004b).

2.2 Boundary layer phenomena

Boundary layer phenomena include the effects of heat exchange with the ground, evaporation from soil, snow, or ice, and slope winds. These effects can result in a thin layer near the ground, from several metres to tens of metres thick, having temperature and humidity significantly different from the air just above. Readings from a weather station immersed in the boundary layer may give a poor indication of conditions just above. Because the boundary layer is thin, its effect on the radiometric temperature of the sky will generally be small in atmospheric windows where astronomical observations can be made. Nevertheless, in some cases even small fluctuations can be important, as when using water vapor radiometry to estimate tropospheric delay (Sutton & Hueckstaedt 1996).

The radiometric signature of a warm, humid boundary layer is frequently observed in daytime FTS spectra obtained on Mauna Kea, Chajnantor, or Sairecabur. On clear days, the sun heats the soil, driving evaporation and convection. Under these conditions, the strongest water lines can be saturated at the line centers within the warm, humid layer of air at ground level, resulting to the appearance of warm features in the spectrum. An example of this effect is shown in Fig. 3.2, below. In contrast, on clear nights, when a surface inversion develops due to radiative cooling of the ground, no analogous cold features are seen, since there is no strong enhancement of the ground level humidity when the soil is cool.

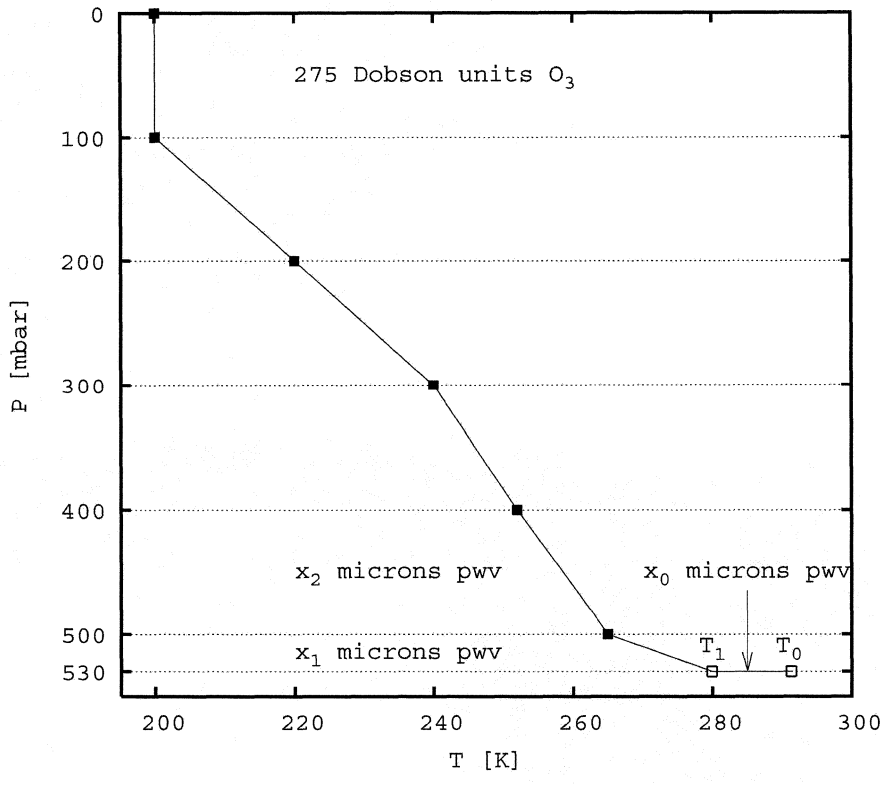

Fig. 3.1 – Schematic of an *am* model layer configuration for fitting FTS spectra at Sairecabur. The atmosphere is divided into 6 layers at the pressure boundaries shown, plus an additional thin, humid, layer at ground level. Fit variables are the three H_2O column densities and two temperatures shown. In addition to H_2O and O_3 indicated, each model layer contains N_2 and O_2 at hydrostatic column density.

3. FTS spectra and modeling

We have developed a general-purpose atmospheric model, *am* (Paine 2004a), for calculating synthetic atmospheric spectra at terahertz frequencies, and for making model fits to measured spectra. A schematic of a simple layer specification for *am*, a representation of the spring daytime atmosphere over Sairecabur, is shown in Fig. 3.1. The layers are defined on a pressure grid, with specified temperatures, derived from Chajnantor radiosonde data, at the layer boundaries. Here, a simple two-step approximation is used to represent the water vapor profile, with an additional thin layer added at ground level to represent the humid daytime surface boundary layer. For the model fit presented here, the three water vapor column densities, as well as the base temperatures of the 500-530 mbar layer and of the surface layer, are designated as fit variables, with all other parameters held fixed.

An example of a fitting run on an FTS spectrum obtained at Sairecabur is shown in Fig. 3.2. The fit clearly demonstrates the validity of the simple layer model described. For the fit, the model spectrum was convolved with the 3 GHz wide resolution function of the FTS. The rms residual is 4.4 K, with much of this coming from the poor signal-to-noise of the FTS spectrum towards low frequencies. The FTS has constant noise per frequency channel, but the thermal radiance from the sky falls of rapidly towards low frequencies, with consequent degradation of the signal-to-noise ratio. Much of the noise is fluctuation noise proportional to the total power admitted to the

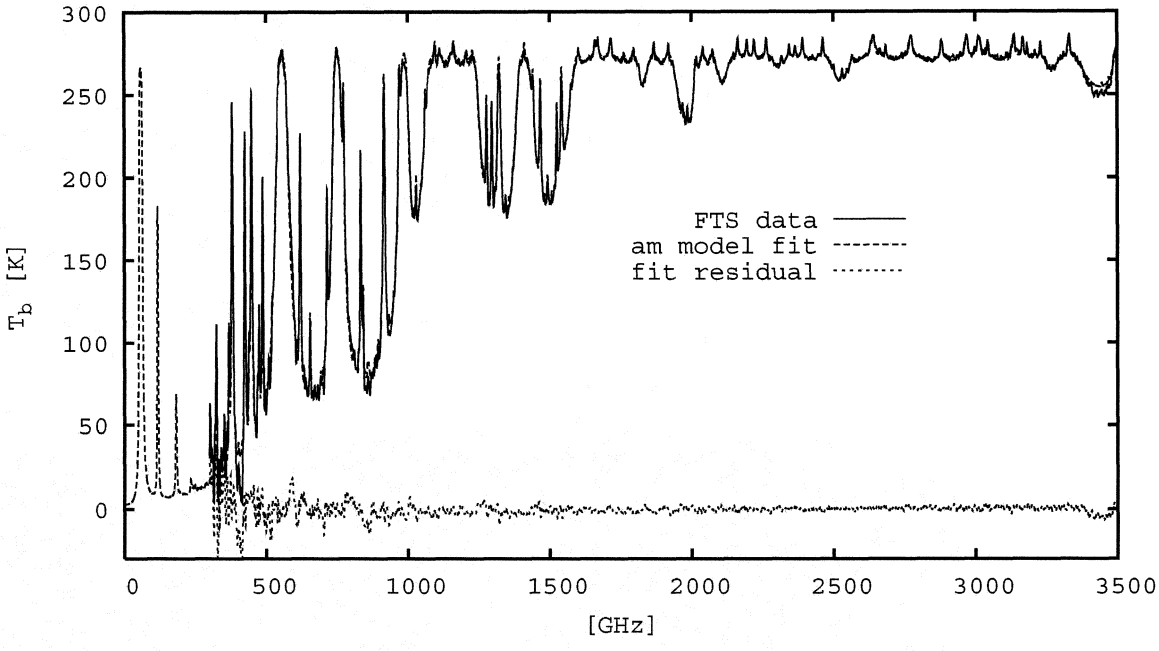

Fig. 3.2 – Sky brightness temperature spectrum measured at Cerro Sairecabur on 2000 Nov 25 at 13:40 UT, and *am* atmospheric model fit using the model layer structure illustrated in Fig. 3.1. The converged parameter values are $T_0 = 291$ K, $T_1 = 280$ K, $x_0 = 0.5$ μm pwv, $x_1 = 47$ μm pwv, $x_2 = 132$ μm pwv (total H_2O column 180 μm pwv).

spectrometer, controlled by filters defining the total spectrometer bandwidth. The low-frequency signal-to-noise ratio could be improved at the expense of high-frequency sensitivity.

3.1 Case Study—10 Nov 1999 FTS and radiosonde measurements at Chajnantor

Beginning in 1998, a collaborative effort was undertaken by Cornell University, ESO, NRAO, and SAO, later joined by the Large Millimeter-Submillimeter Array (LMSA) project, to characterize the atmosphere above the ALMA site at Chajnantor through a series of radiosonde launches. A set of five launches made in the course of a single day on 10 Nov 1999, during which the SAO FTS was simultaneously recording sky brightness spectra at 10-minute intervals, provided an opportunity to make a direct comparison between these two measurements.

Fig. 3.3 shows the water vapor mixing ratio profiles and temperature profiles derived from the radiosonde data for these five radiosonde flights. The water vapor profiles show the characteristic ceilings dividing humid air below and drier air above, associated with relatively weak thermal inversions. During the night, the water vapor ceiling subsides, and the soil cools by radiation in the clear, high altitude conditions, with the associated formation of a surface thermal inversion. The same clear conditions, and tropical latitude, result in substantial solar heating of the soil during the day, with the development of a warm, humid surface layer in the afternoon at 19 UT. The solar heating also drives convection, and the water vapor ceiling rises.

FTS spectra taken over the same period were fitted using a layer configuration and fit parameters similar to Fig. 3.1, with the exception that the ground pressure level was 560 mbar. Also, the surface layer was omitted from the fit for spectra taken at night. In Fig. 3.4, time series of the H_2O column density from ground level to 500 mbar, and the total H_2O column density, are plotted both from the model fits to the FTS spectra, and from the integrated radiosonde H_2O profiles. Both show the same trend associated with the descent of the water vapor ceiling, however the night time radiosondes appear to overestimate the column density somewhat. This overestimate, and the shape of the corners in the H_2O profiles as they approach zero, are indicative of a lag in the humidity sensor response time.

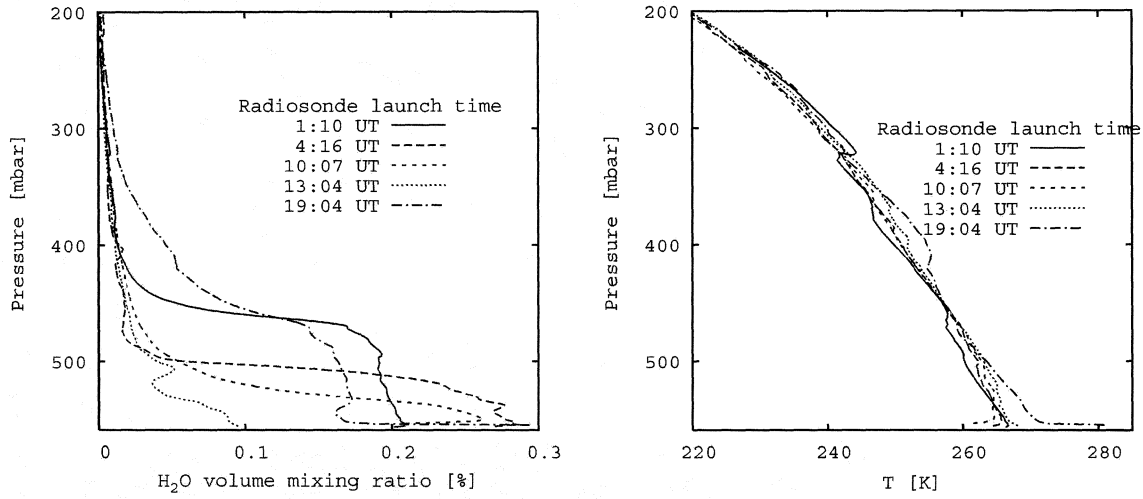

Fig. 3.3 – H_2O volume mixing ratio (left) and temperature profiles (right) from a series of five radiosonde launches at Chajnantor, on 1999 Nov 10. Sun rise, transit, and set times were 9:42 UT, 16:16 UT, and 22:49 UT, respectively.

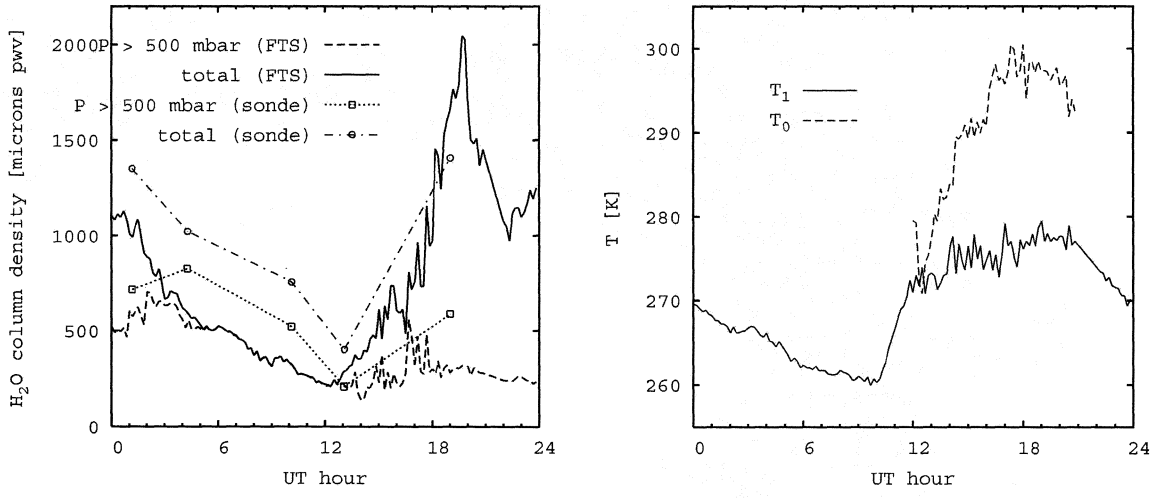

Fig. 3.4 – Time series of model fit parameters for FTS spectra acquired at 10-minute intervals at Chajnantor on 1999 Nov 10. Left: the fitted total pwv, and pwv column from ground level to the 500 mbar level, are displayed. Also shown are the same pwv columns derived from integrating the radiosonde H_2O mixing profiles in Fig 3.3. Right: the fitted base temperatures T_1 and T_0 (daytime only) defined in Fig. 3.1.

To the right in Fig. 3.4, time series are plotted for the fitted layer base temperatures T_0 (daytime only) and T_1 defined in Fig. 3.1. These may be compared with the radiosonde temperature profiles in Fig 3.3 at ground level. Towards sunrise, the fitted T_1 approaches the temperature at the base of the surface inversion measured by the radiosonde at 10 UT, as the water vapor profile descends towards ground level. After sunrise, the steep temperature

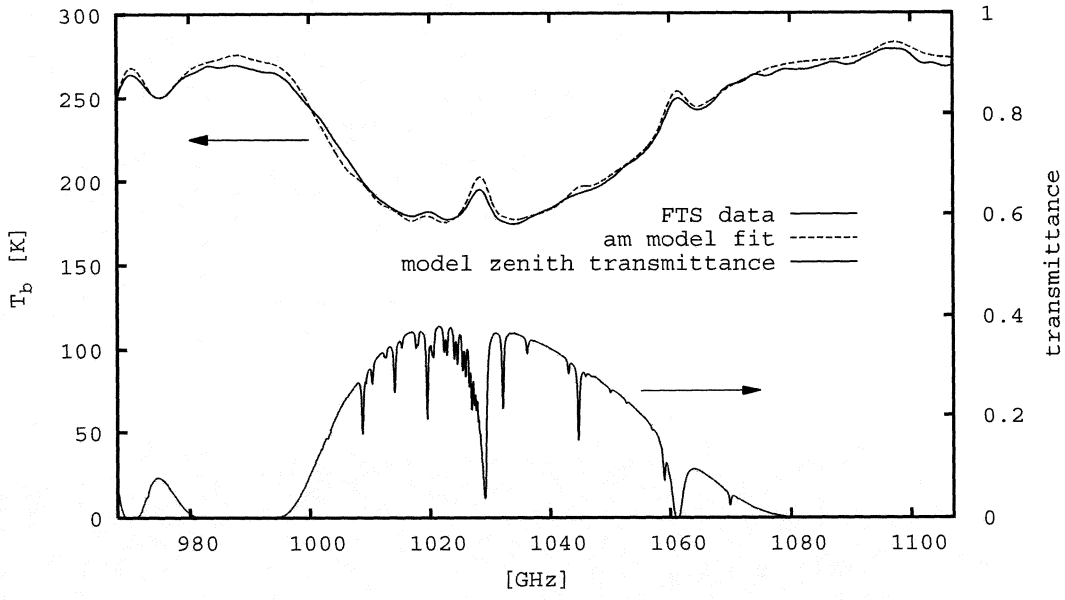

Fig. 4.1 – Model fit, at spectrometer resolution, to FTS sky brightness spectrum, and zenith transmittance spectrum, at full resolution, calculated from the fitted model.

gradient at the surface is well modeled by T_1, which follows the air temperature just above ground level, and T_0, which follows the actual surface temperature. Note that T_0 is higher than the first recorded temperature in the daytime radiosonde temperature profiles, as this point is logged a metre or more above the surface. Between T_1 and T_0, the fitted H_2O column density never exceeds 0.35 μm pwv.

4. Atmospheric calibration for astronomical observations.

The FTS records sky brightness temperature at the zenith. For calibrating astronomical observations, what is needed is the transmittance through the atmosphere at the elevation of the astronomical source. With the model fit in hand, it is a simple matter to recalculate this from the model. Moreover, the recalculation can be done at full resolution, rather than at the broader resolution of the FTS, in this case 3 GHz. This procedure is particularly useful in the neighborhood of unresolved ozone lines. Fig. 4.1 shows an example using the same spectrum from Sairecabur presented in Fig. 3.2, focusing on the 1030 GHz atmospheric window. Several O_3 rotation lines which are unresolved in the FTS spectrum, are resolved in the model calculation.

5. Conclusion

This paper has demonstrated the use of a Fourier transform spectrometer for obtaining a clear picture of the atmospheric conditions above an observatory. This information is invaluable for observations at terahertz frequencies, where the optical depth of the atmosphere is generally high, and where boundary layer phenomena can play a significant role in the radiometric properties of the sky. At the RLT, we have found the FTS to be an essential tool for calibrating the atmospheric transmittance during astronomical observations. It is our belief that operation of a similar instrument at present and future submillimeter and terahertz observatories can offer a significant enhancement to the quality of the observations, and provide useful auxiliary data for use with other site characterization instruments such as atmsopheric phase monitors.

References

Andrews, D. G. 2000, An Introduction to Atmospheric Physics (Cambridge, Cambridge University Press)

Blundell, R. et al. 2003, Proc. Thirteenth Int. Symp. Space Terahertz Tech., p. 159-166

Chamberlin, R. A. 2001, Journal of Geophysical Research (Atmospheres), 106 20,101

Goody, R. M., & Yung Y. L. 1989, Atmospheric Radiation, Theoretical Basis, 2nd ed. (New York, Oxford University Press)

MacDermid, et al. NOAA CMDL Summary Report #25 (1999). Data in Fig. 2.1 have been scaled by 1.25, so that the integrated column matches the typical integrated Dobson column measured from Mauna Loa.

Marrone, D., et al., these proceedings

Paine, S. 2004a, "The *am* Atmospheric Model" SMA Technical Memo #152 rev. 2.0, available at http://sma-www.cfa.harvard.edu/private/memos.

Paine, S. 2004b, "Tropospheric Phase Calibration Using Stratospheric Ozone Line Emission" SMA technical memo, in preparation.

Stark, A. A. et al. 2001, Publications of the Astronomical Society of the Pacific 113, 567

Sutton, E. C., and Hueckstaedt, R. M. 1996, Astron. Astrophys. Suppl. Ser. 119, 559

Yngvesson, S. et al. 2004, these proceedings